Dynamics of Atmospheres and Oceans 65 (2014) 64–85

Contents lists available at ScienceDirect

Dynamics of Atmospheres and Oceans

journal homepage: www.elsevier.com/locate/dynatmoce

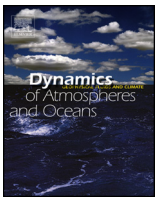

Surface ocean response to synoptic-scale variability in wind stress and heat fluxes off south-central Chile

Catalina Aguirre[a,*], René D. Garreaud[a], José A. Rutllant[a,b]

[a] Departamento de Geofísica, Universidad de Chile, Blanco Encalada 2002, Santiago, Chile
[b] Centro de Estudios Avanzados en Zonas Áridas (CEAZA), Raúl Bitrán s/n, Colina El Pino, La Serena, Chile

ARTICLE INFO

Article history:
Received 11 July 2013
Received in revised form 25 October 2013
Accepted 1 November 2013
Available online 14 November 2013

Keywords:
Atmospheric forcing
Air–sea interaction
Surface currents
Surface temperature
Synoptic variability, Chile

ABSTRACT

The effect of the high frequency (synoptic) variability of wind and heat fluxes upon the surface ocean off south-central Chile (west coast of South America) is investigated using a regional ocean model. We focus our analysis in austral summer, when the regional wind experiences significant day-to-day variability superimposed on a mean, upwelling favorable flow. To evaluate the nature and magnitude of these effects, we performed three identical simulations except for the surface forcing: the climatological run, with long-term monthly mean wind-stresses and heat fluxes; the wind-synoptic run, with daily wind stresses and climatological heat fluxes; and the full-synoptic run, with daily wind-stresses and daily fluxes. The mean currents and surface geostrophic EKE fields show no major differences between simulations, and agree well with those observed in this ocean area. Nevertheless, substantially more ageostrophic EKE is found in the simulations which include synoptic variability of wind-stresses, impacting the total surface EKE and diffusivities, particularly south of Punta Lavapie (37° S), where the lack of major currents implies low levels of geostrophic EKE. Summer mean SSTs are similar in all simulations and agree with observations, but SST variability along the coast is larger in the runs including wind-stress synoptic variability, suggesting a rather linear response of the ocean to cycles of southerly wind

* Corresponding author. Tel.: +56 9 98463933.
E-mail address: catalina@dgf.uchile.cl (C. Aguirre).

0377-0265
http://dx.doi.org/10.1016/j.dynatmoce.2013.11.001

strengthening and relaxation. We found that coastal SST variability does not change significantly in the first tenths of kilometers from the shore when including daily heat fluxes, highlighting the prominent role of wind-driven upwelling cycles. In contrast, in the offshore region situated beyond the 50 km coastal strip, it is necessary to include synoptic variability in the heat fluxes to account for a realistic SST variability.

1. Introduction

Upwelling of cold, nutrient rich waters along much of the Chilean coast induces high primary productivity and maintains one of the major fisheries of the world (e.g., Rutllant and Montecino, 2002; Food and Agriculture Organization, 2004). Coastal upwelling is in turn locally forced by alongshore, southerly (equatorward) winds, being particularly strong around major capes at 30° S (Punta Lengua de Vaca), 33° S (Punta Curaumilla) and 37° S (Punta Lavapié) because of topographic/bathymetric effects (Figueroa and Moffat, 2000). To the north of 33° S upwelling-favorable winds prevail year round whilst off south-central Chile (35–40° S) monthly mean surface winds alternate between moderate northerlies in winter to strong southerlies in summer (DJF), following the seasonal latitudinal migration of the south Pacific anticyclone (e.g. Saavedra and Foppiano, 1992). South of 35° S synoptic variability of the winds is very pronounced in winter – when stronger northerlies are frequent due to the passage of extratropical atmospheric low-pressure disturbances. This high-frequency wind variability is still present in summer (e.g., Sobarzo et al., 2010) due to the quasi-weekly occurrences of southerly coastal low-level jet events alternating with periods of weak southerlies or even northerly flow in connection with the passage of coastal lows (Garreaud and Muñoz, 2005; Garreaud et al., 2002). These jet events are characterized by a meridionally elongated maximum of surface southerly winds over 15 m s^{-1} generally rooted in Punta Lavapié and extending northward several hundreds of km (Muñoz and Garreaud, 2005; Montecinos et al., 2011). Consistent with the mean upwelling-favorable winds due to the southernmost position of the subtropical anticyclone and the occurrence of strong atmospheric low-level coastal jets, the region around Punta Lavapié exhibits the highest primary productivity along the Chilean coast during summer (e.g., Montecino et al., 2006).

Although the basic features of coastal upwelling, including their regional distribution and seasonal variability, have been described elsewhere (e.g., Figueroa and Moffat, 2000; Leth and Shaffer, 2001; Blanco et al., 2001; Sobarzo et al., 2007), there is less information on the surface ocean response to atmospheric low-level jet events, partly because of the scarcity of in situ data. Using satellite observations Renault et al. (2009) studied the effect of the atmospheric low-level jet on sea surface temperature (SST) off central Chile (30° S), but the blind zone close to the coast was an important limitation to capture the upwelling response to the wind forcing which is particularly important within the first 20 km off the coast (e.g., Perlin et al., 2007; Aiken et al., 2008). Modeling efforts have also been conducted to understand upwelling and ocean circulation off central Chile (Batteen et al., 1995; Leth and Shaffer, 2001; Mesias et al., 2001, 2003; Leth and Middleton, 2004; Aiken et al., 2008). However, most of these studies have used climatological (long-term-mean) wind data to force an ocean model, perhaps missing an important source of variability, particularly south of 35° S in austral summer. Only Mesias et al. (2001) and Aiken et al. (2008) used daily wind data, but the former utilized a coarse horizontal resolution (2.5° × 2.5° lat–lon grid) and the latter applied a spatially homogeneous wind stress field, as derived from records at a single coastal station. The lack of spatial structure of the near-shore winds in both studies may strongly influence the patterns of the circulation and SST (Capet et al., 2004). Recently, Renault et al. (2012) modeled the upwelling response to an atmospheric low-level jet event that occurred in spring off north-central Chile (30° S), focusing on the spatial variability of the forcing wind field.

Here, we used the Regional Ocean Modeling System (ROMS) (Shchepetkin and McWilliams, 2005) off Chile to investigate the impact of quasi-weekly atmospheric low-level jet events on the surface ocean through wind-stress and heat flux forcing. Three runs of the model were forced by different

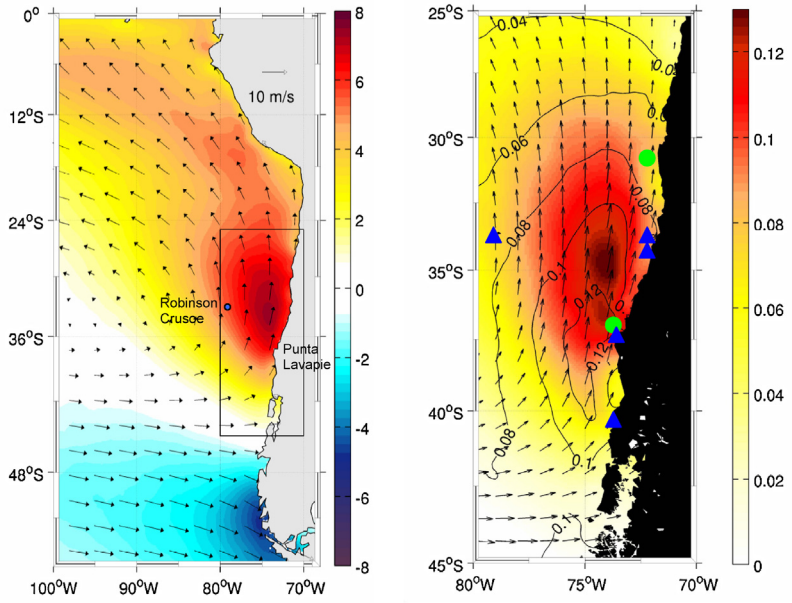

Fig. 1. (a) Climatology of the austral summer (DJF) meridional wind (colors, in m s^{-1}) and wind vector (vectors) from QuikSCAT (2000–2007) in the South East Pacific. The rectangle indicates the model domain of the ROMS simulations used in this study. (b) Climatology of the austral summer (DJF) meridional wind stress (colors, in Pa), standard deviation of the meridional wind stress (contours) and wind stress vector (vectors) from QuikSCAT (2000–2007) in the model domain. In addition, green dots and blue triangles indicate the current meter moorings and thermistor locations respectively. (For interpretation of references to color in the figure legend, the reader is referred to the web version of this article.)

surface conditions. A *climatological run* was performed using long-term-mean monthly wind-stresses, similar to previous studies. The other two simulations were forced by daily wind-stresses (momentum fluxes), but only one of them allowed for day-to-day changes in heat fluxes. This experimental set up allowed us to gauge the nature and magnitude of the surface ocean variability induced by varying surface heat fluxes and wind stresses separately. Although the model domain extends along most of the Chilean coast (25–45° S) and the runs span 8 full years, we focus our study off south-central Chile (35–40° S) during austral summer, when there is significant synoptic variability in the wind superimposed on a mean, upwelling-favorable flow (Fig. 1b).

The rest of the paper is organized as follows: Section 2 describes the model, its configuration, the experiments performed and the data sets used for validation; Section 3 focuses on comparison between simulations and their validation using available satellite and in situ observations of mean fields and variability of currents and SST. This is followed by a discussion in Section 4. Finally, Section 5 includes a summary of the main results and conclusions.

2. Methods and model

2.1. Model configuration and experimental setup

This study used the Regional Oceanic Modeling System (ROMS AGRIF v.2.1), a split-explicit, free surface, topography-following-coordinates oceanic model that solves the primitive-equations assuming hydrostatic and incompressible conditions (Shchepetkin and McWilliams, 2005). Radiation conditions are used in open boundaries in order to treat the inward and outward information fluxes separately. When information fluxes are outward the boundary is passive and when they are inward the boundary is active, nudging toward its lateral boundary conditions (Marchesiello et al., 2001). Sponge layers of 70 km width, which are regions of increased horizontal viscosity (maximum value of 800 m^2 s^{-1}), were

Table 1
Surface forcing and spatial/time resolution of the different simulations performed in this work.

Variable	Climatological (CL)	Wind-synoptic (WS)	Full-synoptic (FS)
Wind stress	Climatological QSCAT	Daily QSCAT	Daily QSCAT
Wind velocities	Climatological COADS	Climatological COADS	Daily QSCAT
Air temperature, relative humidity, precipitation, radiation	Climatological COADS	Climatological COADS	Daily NCEP
Boundary and inicial conditions	Climatological WOA	Climatological WOA	Climatological WOA
Spatial resolution	1/10°	1/10°	1/10°
Outputs time resolution	Daily	Daily	Daily

used near open boundaries. The vertical mixing is parameterized using a K-Profile Parameterization (KPP), a non-local closure scheme based on the boundary layer formulation by Large et al. (1994).

To analyze the effect of the synoptic-scale variability in wind stresses and surface heat fluxes relative to a smooth mean seasonal variation, we performed three simulations (termed as *climatological*, *wind-synoptic* and *full-synoptic*) that only differ in their surface boundary conditions. The model domain spans from 25° to 45° S and from 70° to 80° W, where the northern, western and southern boundaries are open (Fig. 1). Climatological monthly means of temperature and salinity obtained from the World Ocean Atlas 2005 (Locarnini et al., 2006; Antonov et al., 2006) were used to nudge the circulation at the three open boundaries. These data were used to estimate climatological values of geostrophic currents considering a level of no motion at 1000 m depth. The model horizontal resolution is 1/10°, which corresponds to ~7.9–10.1 km, with a 248 × 101 grid. The bathymetry was extracted from the 2′ resolution ETOPO database (Smith and Sandwell, 1997). In spite of the fact that the model prevents large errors in the computation of horizontal pressure gradients in the ocean (Shchepetkin and McWilliams, 2003), the bathymetry (h) was smoothed in order to maintain a "slope parameter" $r = \nabla h/2h < 0.25$ (Beckmann and Haidvogel, 1993). The grid has 32 vertical levels and stretching parameters of $\theta_s = 7$, $\theta_b = 0$ and $hc = 10$ m (Song and Haidvogel, 1994), allowing for a good representation of the surface ocean. The time step was 13.3 min and outputs were averaged over each day.

The *climatological* run (CL) used long-term monthly mean wind stresses (between 2000 and 2007) as a surface boundary condition, calculated from QuikSCAT data from the Center d′Exploitation et de Recherche Satellitaire (CERSAT), at the Institut Francais de Recherche pour l'Exploitation de la Mer (IFREMER), along with climatological monthly means of short and long wave radiation fluxes, air temperature, humidity, precipitation and wind speeds from the Comprehensive Ocean-Atmosphere Data Set (COADS) (Da Silva et al., 1994) to calculate the surface heat and freshwater fluxes. This simulation was integrated for 10 years of 360 days each, repeating the mean annual cycle of the surface forcing. Statistics were analyzed for the last 8 years (the first 2 years are considered model spin-up). The *wind-synoptic* run (WS) was forced with daily wind-stresses from QuikSCAT data (between 2000 and 2007), but used climatological COADS data to calculate surface fluxes, as in the CL run. Finally, the *full-synoptic* simulation (FS) was the experiment with more realistic surface boundary conditions (in terms of variability), because it was forced with daily QuikSCAT wind-stresses and daily heat and freshwater fluxes calculated from daily surface variables. Time series with 6-h resolution from 2000 to 2007 of short and long wave radiation fluxes, air temperature, humidity and precipitation were obtained from the NCEP Climate Forecast System Reanalysis (CFSR) with a spatial resolution of 0.3° (Saha et al., 2010). This is a new coupled global NCEP Reanalysis at much higher temporal and spatial resolution than the previous Reanalysis (Kalnay et al., 1996). The major advantages of using this new data set are the coupling to the ocean during the generation of the 6-h fields and higher spatial resolution permitting analyses closer to the coast. These time series were daily averaged to calculate (through bulk formulas) surface heat and fresh water fluxes using daily wind speeds from QuikSCAT in the same period. Both WS and FS had an initial two year integration using surface boundary forcing for the year 2000 (spin-up period). Thus, we computed model statistics using 8 years, as in CL. Table 1 summarizes the three experiments performed in this study.

Table 2
Information about the moorings and measurements.

Site	Latitude	Longitude	Start time	End time	Δt (min)	Depth range measurement	Bin size	Water depth
COSMOS	30°21′ S	71°47′ W	April 2003	September 2006	60	10–110 m	5 m	950 m
Station 18	36°28′ S	73°10′ W	January 2009	January 2011	30	6–86 m	4 m	100 m

2.2. Data sets for validation

We used both satellite and in situ data to validate the simulated SST and currents. To test our model summer mean surface geostrophic currents and their variability (geostrophic EKE), we used the altimetry-derived gridded product (1/3°) of the geostrophic current anomalies from the Archiving, Validation and Interpretation of Satellite Oceanographic Data (AVISO) spanning from 2000 to 2007. The absolute surface velocity is obtained by adding a mean estimated geostrophic current based on dynamic heights using temperature and salinity climatologies from CARS 2009 (CSIRO Atlas of Regional Seas) (Ridway et al., 2002; Dunn and Ridgway, 2002), considering 1000 db as the reference level.

To validate the model summer mean velocity vertical profiles near the coast, in situ current measurements were used. Current data were obtained from two moorings (Fig. 1b) located ∼13 km from the shore on the continental slope at 30°S (COSMOS) and ∼20 km from the shore on the continental shelf at 36.5° S (Station 18). Both moorings, maintained by the Center for Oceanographic Research in the eastern South Pacific (COPAS), were instrumented with a 300 kHz acoustic Doppler current profiler (ADCP) pointing upward. Table 2 lists the positions, start and end times of the current meter records and the depth of the water column.

The simulated summer mean SST field is compared to the summer mean (years 2000–2007) SST obtained from the Advanced Very High Resolution Radiometer (AVHRR), specifically the Pathfinder Version 5.0 SST Project (Pathfinder V5) product. This data set has a spatial resolution of ∼4 × 4 km and it is distributed by the Physical Oceanography Distributed Active Archive Center (PO.DAAC).

Observations of offshore synoptic SST variability field were obtained from the TRMM Microwave Imager (TMI) data set produced by Remote Sensing Systems (RSS). These data were used to compare with the simulated synoptic SST variability. This product is largely uninfluenced by cloud cover, aerosols and atmospheric water vapor (Wentz et al., 2000). Daily satellite SST fields between 2000 and 2007 on a regular grid of 0.25° for latitudes lower than ∼38° S were used. Since the TMI blind zone corresponds to the first 50 km from the coast, modeled coastal SST had to be validated against in situ data recorded by near surface thermistors at four different locations (Fig. 1b). These daily SST data were provided by the Servicio Hidrográfico y Oceanográfico de la Armada de Chile (SHOA) at Valparaíso (33° S–71.6° W), San Antonio (33.6° S–71.5° W), Talcahuano (36.7° S–73.1° W), Corral (39.9° S–73.4° W) and Robinson Crusoe Island (33.6° S–78.8° W).

3. Simulations inter-comparison and validation

3.1. Mean circulation

The summer mean surface geostrophic currents obtained from both satellite altimetry and model sea level output reveal a well-defined equatorward flow and jet-like structure (Fig. 2). This flow has previously been described using altimetry data (Fuenzalida et al., 2008) showing higher equatorward velocities during summer. The dynamics of the seasonal cycle of this jet is probably related to the spring/summer intensification of the wind-stress curl which produces a surface equatorward current via thermal wind balance (Aguirre et al., 2012). Since our three simulations contain the same seasonal variations in the wind-stress field (from QuikSCAT), we obtain a similar geostrophic equatorward flow with a mean value of ∼12 cm s^{-1} during summer. Nevertheless, this jet exhibits a more coherent structure in the FS simulation. The simulated ocean jet evidences a coastal separation near Punta Lavapié, an important feature that has been observed in hydrographic data (Letelier et al., 2009) confirming

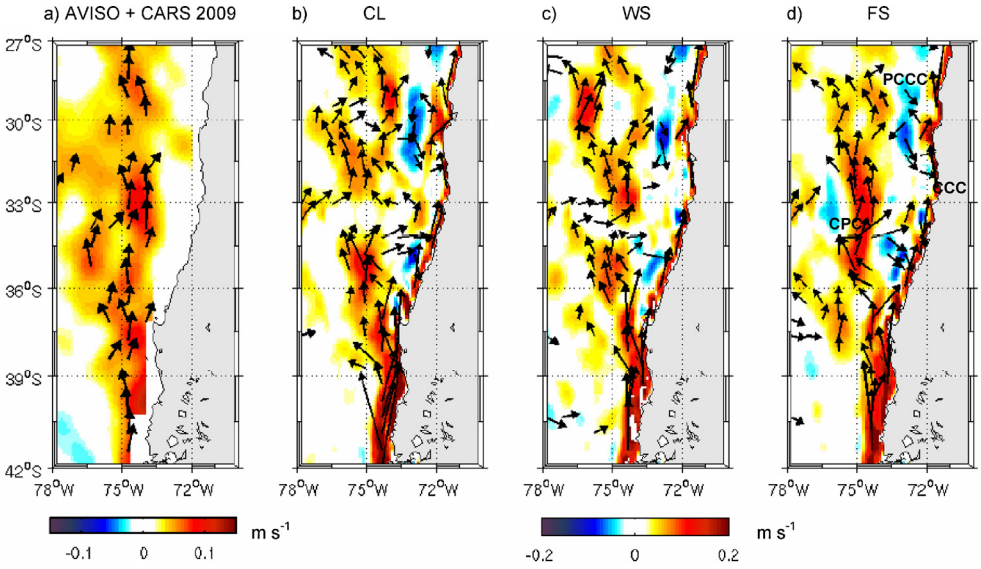

Fig. 2. Climatology of the austral summer (DJF) surface geostrophic meridional currents (colors) obtained from (a) a combination of mean surface geostrophic currents based on CARS temperature and salinity climatology (assuming a level of no motion at 1000 db) and geostrophic current anomalies derived from AVISO altimetry; and (b)–(d) surface geostrophic meridional currents obtained from the three different simulations. Vectors are shown only if the current speeds are higher than 5 cm s^{-1}. (For interpretation of references to color in the figure legend, the reader is referred to the web version of this article.)

previous simulations with the Princeton Ocean Model (Mesias et al., 2001, 2003; Leth and Middleton, 2004). The model velocities are somewhat higher than satellite-derived surface currents (>10 cm s^{-1}) and show more spatial structure than observations, but it is important to note that altimetry data is smoothed in the process of creating gridded fields from multiple altimeters.

The model alongshore flows reproduce the major features of the circulation in the southeast Pacific (Figs. 2 and 3) as identified by Strub et al. (1998). The Chile-Perú surface Current (CPC, also known as the Humboldt Current) is the eastern branch of the subtropical South Pacific gyre. As mentioned above it intensifies during austral summer. The Chile Coastal Current (CCC), flowing equatorward as an ocean coastal jet (speeds larger than 25 cm s^{-1}), is related to upwelling dynamics (e.g., Aiken et al., 2008). The model clearly captures the mean CCC with a cross-shore scale of about 40 km off south-central Chile and speeds in the 15–25 cm s^{-1} range.

The Perú-Chile Countercurrent (PCCC) is a surface poleward flow located about 100–300 km west of the CCC (Strub et al., 1995). This current has been described using satellite-derived sea-surface height anomaly data, showing a maximum during austral spring and a minimum in fall. In our simulations a mean poleward surface current, consistent with the observed location of the PCCC, is found during summer north of 33° S with speeds of about 5 cm s^{-1}. Finally, the Perú-Chile Undercurrent (PCU) is a well-defined poleward flow located over the continental shelf and continental slope (Shaffer et al., 1997, 1999; Pizarro et al., 2002). The vertical sections of our simulations (Fig. 3) reproduce the PCU with summer means in excess of 10 cm s^{-1} at 30° S and weaker at 36.5° S (~5 cm s^{-1}). The mean value obtained at 30° S (12 cm s^{-1}) agrees well with the annual mean value of 13 cm s^{-1} obtained for a six year period of current measurements near the PCU core over the slope at 30° S (Shaffer et al., 1999).

Cross sections of the model alongshore flow with depth at 30.3° and 36.5° S are contrasted with the near surface circulation described for the Chile-Perú Current System. At 30° S the three simulations of the summer mean alongshore currents (i.e. meridional *V* components) do not show major differences in their structure and intensity. Only the PCCC current is slightly weaker in the WS simulation (Fig. 3a). At 36.5° S the three simulations of the coastal mean alongshore currents are very similar, differences being only observed in the intensity of the northward flow west of the 100 km coastal strip.

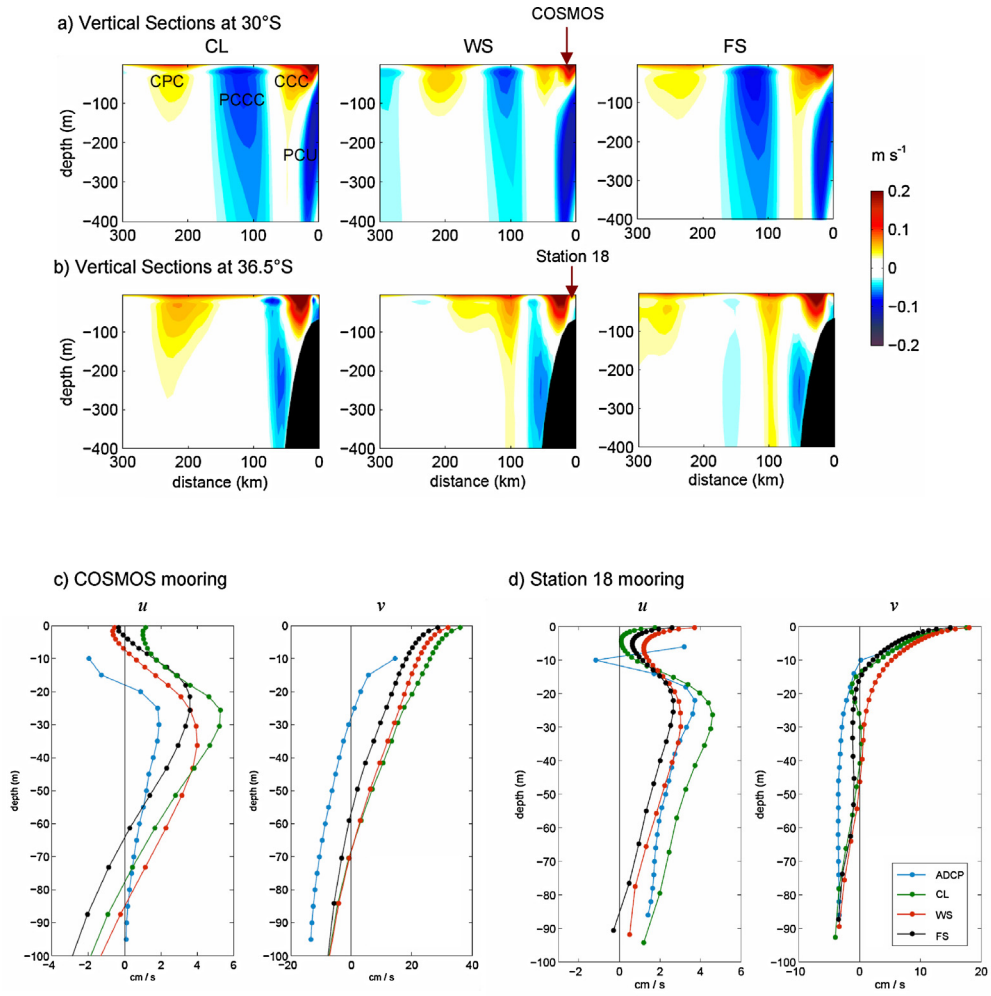

Fig. 3. Mean vertical sections of the simulated summer meridional currents for the three different simulations at (a) 30° S and (b) 36.5° S. Labels indicate the location of the major current systems (see text for details) and arrows indicate the position of the moorings. Summer mean profiles of the meridional (v) and zonal (u) currents at the moorings (c) COSMOS and (d) Station 18.

Further verification of the model performance in simulating the summer mean currents is provided in Fig. 3c and d by the summer mean vertical profiles of zonal (u) and meridional (v) components along with their observational counterparts obtained from two ADCP (see Section 2.2). As found before, mean profiles from our three simulations are very similar, their shapes agree well with the observations and they capture, in general, the reversal of the currents at different depths. The agreement is better in S18, within our target area, while farther north (COSMOS) the model profiles show an overestimation of the northward and eastward surface current. Note that the averaging period differ between observations and simulations.

The model ageostrophic component of the surface flow was estimated by subtracting the geostrophic currents (obtained from the model sea level) from the total currents. The summer mean of the ageostrophic currents is very similar in our three simulations (not shown) and it is largely explained by the surface Ekman currents obtained directly from the wind data (Fig. 4a). Nevertheless friction,

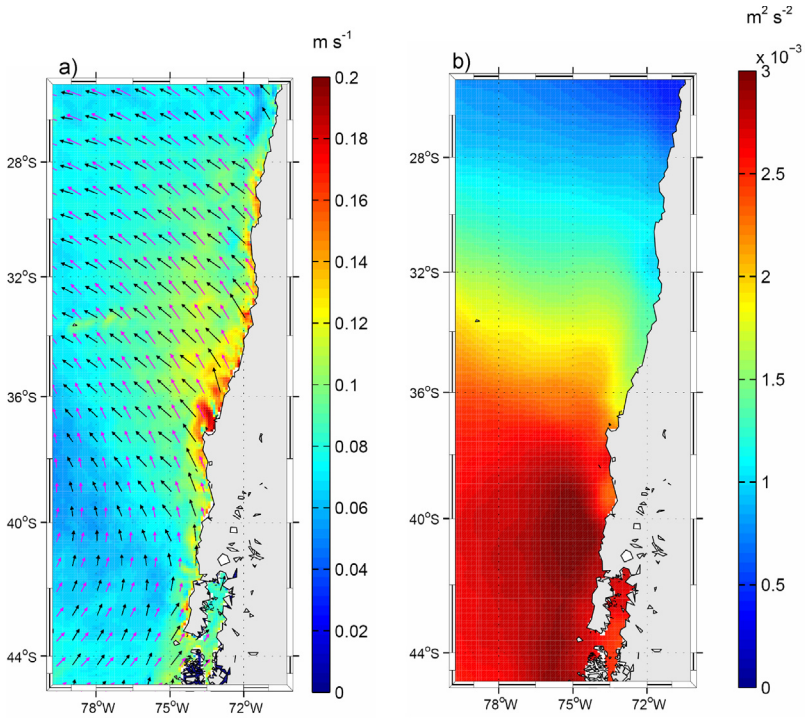

Fig. 4. (a) Summer mean of the surface ageostrophic currents speed (colors) and ageostrophic currents vector (black vectors) from the model (FS). Magenta vectors correspond to the summer mean of the Ekman surface currents obtained directly from the QuikSCAT wind stress field. (b) Summer mean of the ageostrophic EKE obtained from the Ekman surface currents calculated from daily QuikSCAT wind stresses. (For interpretation of references to color in the figure legend, the reader is referred to the web version of this article.)

along with non linear interactions increase the ageostrophic currents close to the coast, departing from the Ekman theory (Ekman, 1905).

3.2. Eddy kinetic energy (EKE)

Given the complexity in the EKE generation, surface EKE comparison between a model and data is a stringent test of the upper-ocean circulation (Capet et al., 2008). To test our simulations, we compared them to altimetry-derived geostrophic EKE (see Section 2.2). The model outputs allow calculation of both total EKE (time average of the square of sea surface velocity departures from the mean) and geostrophic EKE (obtained from the sea-surface height anomalies).

In general, in the offshore region, the spatial pattern of geostrophic EKE is similar in the three simulations and in agreement with satellite data (Fig. 5). Higher values are found in a band rooted along the coast between 38 and 30° S. This region corresponds to the energetic coastal transition zone off Chile described by Hormazabal et al. (2004) using 7.5 years of AVISO data. Although our simulations do not capture the high geostrophic EKE centered at 76° W–28° S which is observed in satellite altimetry, this is probably due to the closeness of this feature to the domain boundary, being therefore affected by the sponge layer, the model and observed geostrophic EKEs show higher values in a band extending offshore in a NW direction from Punta Lavapie, consistent with the coastal jet separation. This feature has recently been observed in the surface vorticity field of a regional coupled model in the Southeast Pacific (Putrasahan et al., 2013). The offshore values of the simulated geostrophic EKE are, however, 40 and 60% larger than the observations, an overestimation also found in other upwelling systems (Veitch et al., 2010; Capet et al., 2008). This could be attributed, in part, to a smoothing of the gridded AVISO

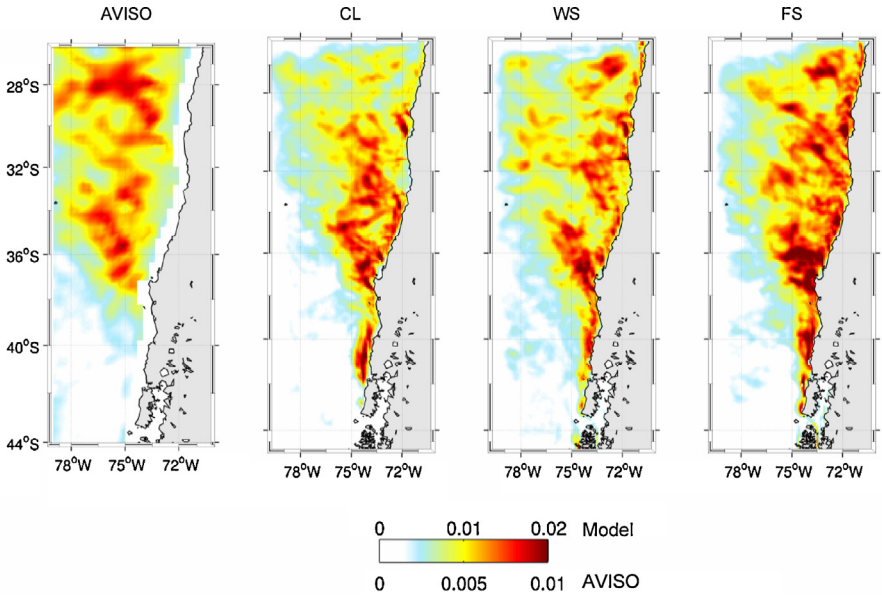

Fig. 5. Summer mean of the geostrophic surface eddy kinetic energy (EKE, $m^2\ s^{-2}$) derived from AVISO data and from the three different simulations.

data. In particular, the observed geostrophic EKE minima close to the coast, could be attributed to the nearshore eddy scale (<50 km) not resolved in the satellite data (Ducet et al., 2000). Furthermore, to the south of 37° S the simulations exhibit high geostrophic EKE (~150 $cm^2\ s^2$) in a coastal strip of about 70 km wide that is not present in the observations, probably because AVISO data are not reliable within the first ~50 km offshore.

In contrast to the geostrophic EKE, the ageostrophic kinetic energy of the CL (obtained from the ageostrophic currents) is significantly different from both PS and FS (Fig. 6). The simulations forced with daily wind stress data exhibit a coastal band of high ageostrophic EKE (>50 $cm^2\ s^{-2}$) from 35 to 45° S accounting for about 25% of the total surface EKE. A coastal band of high ageostrophic EKE is also found in the CL, but with smaller spatial extent and with weaker values (~15 $cm^2\ s^{-2}$) than in WS and FS. In general, ageostrophic EKE in the CL represent less than 5% of the total EKE. A similar spatial pattern and values were found in a climatological simulation for the California Current System, where a coastal strip of intensified ageostrophic EKE would result from nonlinear advection of momentum in the upwelling dynamics (Marchesiello et al., 2003).

South of the jet separation (i.e. south of Punta Lavapie), the offshore region exhibits the weakest geostrophic EKE due the lack of a major current inducing baroclinic instability. In fact, values of geostrophic EKE in this region remain below 50 $cm^2\ s^{-2}$ [Hormazabal et al., 2004]. Thus, as a consequence of the synoptic variability in the wind in this region, the ageostrophic EKE becomes particularly important by contributing to the total EKE, as much as 30–50% in the WS and 40–60% in the FS simulations. In fact, the ageostrophic EKE produced by the Ekman currents is maximum south of Punta Lavapie (Fig. 4b).

Therefore, variable winds enhance the level of eddy kinetic energy in the coastal zone and principally in the nearshore south of ~37° S over a background EKE which is independent of the wind stress temporal resolution.

3.3. *Lagrangian properties of the surface flow*

We have shown that forcing ROMS with synoptic-scale variable winds and heat fluxes makes little difference in the resulting mean currents and geostrophic EKE compared with a smooth

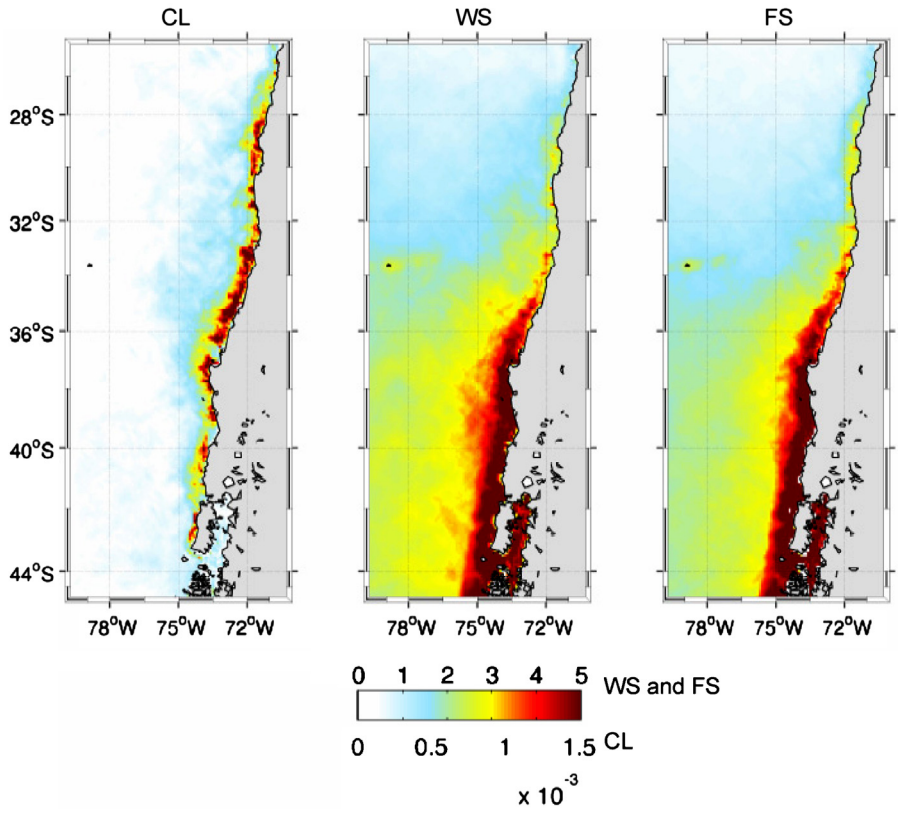

Fig. 6. Summer mean of the ageostrophic surface eddy kinetic energy (EKE, $m^2\ s^{-2}$) obtained from the three different simulations.

(climatological) forcing, but it does increase the ageostrophic EKE along the coast and, particularly, in the offshore region south of Punta Lavapie (Fig. 4b). To further quantify this effect, we studied the properties of the surface flow by tracking particles released at the surface using a Lagrangian drifter-tracking code, developed by X. Capet[1]. The offline version of the code advects numerical floats from stored ROMS outputs of the velocity field. For more details of the algorithm the reader is referred to Carr et al. (2008). For this analysis we used the ROMS outputs from December of each simulated year (8 months per simulation). Drifters were released simultaneously at the surface within a strip of ~25 km wide located about 200 km from the shore, separated by 5 km in the cross-shore direction and 10 km in the along-shore direction (Fig. 7). This analysis was performed in a region with high EKE north of Punta Lavapie (centered at 35° S) and in a region with low EKE south of Punta Lavapie (centered at 43° S).

One interesting result is that some drifters migrate to the coast if synoptic wind variability is used. Even more drifters go to the coast if the heat flux variability is added, particularly at the southern region. These results stress the advantage of using variable winds and heat fluxes to force ocean models, eventually coupled with biological models to describe the ocean upper circulation and its impact on the marine populations.In a Lagrangian frame, the velocity vector of each drifter ($\mathbf{U}(t)$) can be written as $\mathbf{U}+\mathbf{u}'(t)$, where $\mathbf{U}$ is the mean flow, representative of the large spatial scale and

[1] ROMS offline floats (Roff) available at http://www.atmos.ucla.edu/~capet/Myresearch/my_research_floats.html.

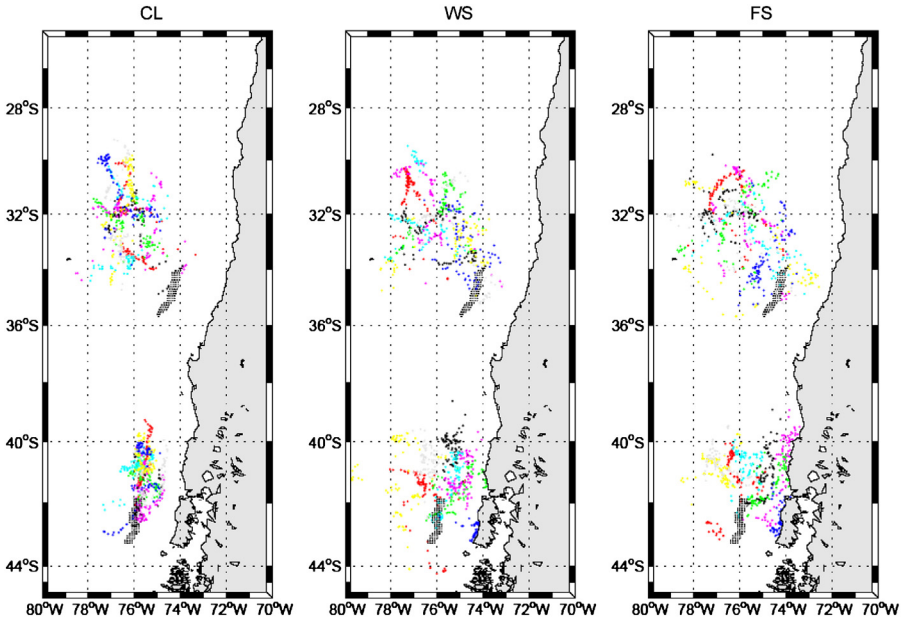

Fig. 7. Dispersion of surface drifters in two different locations off south-central Chile. The black dots indicate the initial position of the drifters and dots with different colors represent the position reached by each drifter one month later (December) in different years of simulation. (For interpretation of references to color in the figure legend, the reader is referred to the web version of this article.)

calculated by averaging the velocity components over each drifter trajectory, and $\mathbf{u}'(t)$ is the time varying perturbation (e.g., Kundu and Cohen, 2000). For the zonal (u') and meridional (v') components of the eddy velocity we calculated the integral time scale $\boldsymbol{T}=(T_u,T_v)$ as

$$T_{u,v} = \frac{1}{R_{u,v}(0)} \int_0^{\Gamma} R_{u,v}(\tau) d\tau$$

where $R_{u,v}(\tau)$ is the Lagrangian autocovariance function and Γ is the lag at first zero crossing (e.g., Chaigneau and Pizarro, 2005). The autocovariance and integral times were computed for each drifter spending the complete month inside the domain (80 drifters in each simulation). The integral length scale $\mathbf{L}=(L_u,L_v)$ and the horizontal diffusivity $\mathbf{K}=(K_u,K_v)$ was obtained using [e.g., Chaigneau and Pizarro, 2005]:

$$\mathrm{L} = \sqrt{\overline{\mathrm{u}'^2}} \cdot \mathrm{T}$$

$$\mathrm{K} = \overline{\mathrm{u}'^2} \cdot \mathrm{T}$$

The results of these statistics are presented in Table 3. On the basis of a t-test with a significance level of 5%, all mean values are significantly different between the north and south regions of release (i.e. north and south of Punta Lavapie). Most importantly, south of Punta Lavapie all mean values are significantly different between CL and WS simulations. This is not the case north of Punta Lavapie, where we did not find significantly different T_u, L_v and diffusivities. Moreover, south of Punta Lavapie diffusivities are significantly different between WS and FS (at 95% confidence level). In terms of the diffusivity magnitude ($|\mathbf{K}|$) we found similar differences between absolute values of $\mathbf{K}$ between CL and WS in both regions ($\sim 0.5 \times 10^7$ cm^2 s^{-1}), but their relative importance to the total diffusivity differ considerably. Variable winds increase diffusivity by only 14% in the north part, contrasting with 71%

Table 3
Lagrangian time (T_u,T_v) and length (L_u,L_v) scales, velocity variances ($\overline{u'^2}$, $\overline{v'^2}$) and diffusivities (K_u,K_v) for the zonal and meridional components of the surface flow in three different simulations and for two different location for the numerical drifter release (see more details in the text).

Simulation	Float release	T_u, days	T_v, days	L_u, km	L_v, km	$\overline{u'^2}$, cm^2 s^{-2}	$\overline{v'^2}$, cm^2 s^{-2}	K_u, 10^7 cm^2 s^{-1}	K_v, 10^7 cm^2 s^{-1}
CL	35° S	3.01 ± 0.07	3.86 ± 0.06	24.8 ± 1.2	20.6 ± 0.7	95	77	2.75 ± 0.22	1.88 ± 0.98
	43° S	3.39 ± 0.06	3.68 ± 0.08	10.9 ± 0.4	12.5 ± 0.6	15	17	0.46 ± 0.02	0.59 ± 0.05
WS	35° S	3.04 ± 0.06	2.99 ± 0.06	27.3 ± 1.1	21.9 ± 0.9	112	75	2.71 ± 0.17	2.22 ± 0.14
	43° S	2.20 ± 0.05	2.26 ± 0.05	14.0 ± 0.4	11.3 ± 0.4	54	37	1.07 ± 0.05	0.73 ± 0.04
FS	35° S	2.71 ± 0.06	3.06 ± 0.08	25.0 ± 1.0	24.7 ± 1.1	120	89	2.95 ± 0.18	2.52 ± 0.19
	43° S	2.16 ± 0.04	2.25 ± 0.06	13.0 ± 0.4	12.3 ± 0.6	50	44	0.95 ± 0.04	0.94 ± 0.08

The diffusivities obtained by Chaigneau and Pizarro (2005) using drifter buoy trajectories in the CPC region (24°–34°S;70°–82°W) were $K_u = 2.2 \pm 0.5$ $(\times 10^7)$ cm^2 s^{-1} and $K_v = 1.8 \pm 0.4$ $(\times 10^7)$ cm^2 s^{-1}.

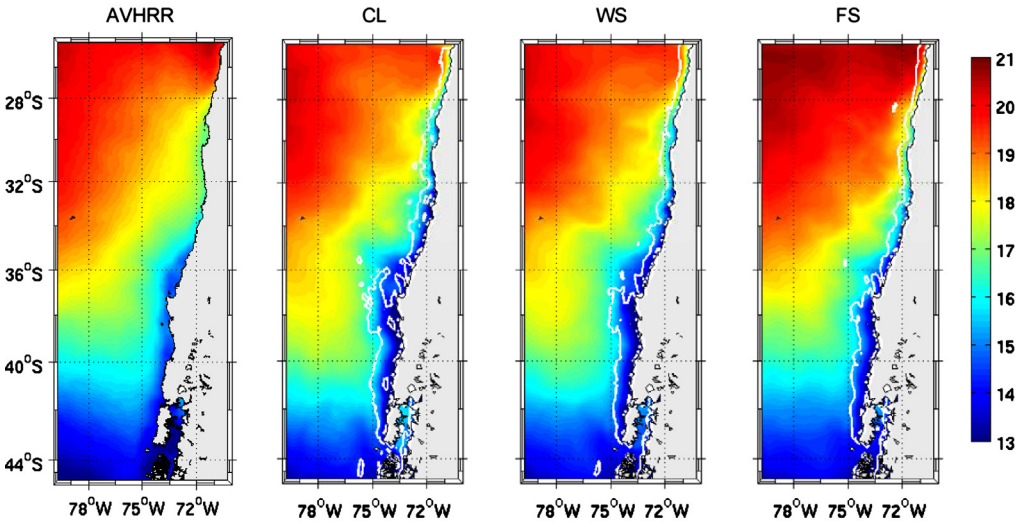

Fig. 8. Summer mean of the sea surface temperature (°C) from satellite observations (AVHRR, Pathfinder Version 5.0) and the three different simulations (2000–2007). White lines in model SST field indicate the location of the mean coastal upwelling front.

in the south part of the domain. On the other hand, the inclusion of synoptic variability in the heat fluxes only accounts for an increase of 3% in the magnitude of the diffusivity in both regions.

Tracking actual drifters in the region between 24°–34° S and 70°–82° W, Chaigneau and Pizarro (2005) obtained annual mean diffusivities of $K_u = 2.2 \pm 0.5$ $(\times 10^7)\,\mathrm{cm^2\,s^{-1}}$ and $K_v = 1.8 \pm 0.4$ $(\times 10^7)\,\mathrm{cm^2\,s^{-1}}$. These values are lower than K-values obtained in our FS simulation, but it is important to note that we calculate diffusivities only for summer in a region south of the Chaigneau and Pizarro (2005) estimate, where synoptic-scale variability in the winds is higher.

3.4. Sea surface temperature

The mean of the summer SST observed from the Advanced Very High Resolution Radiometer (AVHRR, Pathfinder V5) and those simulated (2000–2007) in the three different runs are presented in Fig. 8. Our three simulations are able to reproduce a realistic pattern of the summer mean SST field, with warmer waters offshore and colder waters along the coastal region, superimposed on a general NW-SE decrease in SST. The simulated summer upwelling front (i.e., the offshore limit of the coastal highest SST gradient) is about 75 km from the coast north of Punta Lavapie and ~100 km from the coast south of Punta Lavapie. These values are in agreement with the estimated location of the front using satellite observations (Letelier et al., 2009).

While in the offshore region of south-central Chile simulated summer SST is less than 1 °C warmer than satellite observation, close to the coast the CL and WS summer SST means are 2–3 °C colder than satellite observations (Fig. 9). However, these differences reduce to ~1° C in the FS, a condition that cannot be directly attributed to variability in the heat fluxes, since the input atmospheric variables are different for COADS (used in CL and WS) and NCEP (used in FS). A colder bias along the coast has also been reported in climatological simulations of the Benguela upwelling system (Penven et al., 2001; Veitch et al., 2010) and the Perú upwelling system (Penven et al., 2005), attributed to the low spatial resolution of the wind forcing. In our case, the wind stress over the first ~50 km off the coast was simply extrapolated from the nearest QuikSCAT ocean grid point (0.5° grid spacing), typically resulting in an overestimation of the wind speed, and hence Ekman transport, in the near shore coastal strip (Capet et al., 2004). Assumption of a given cross-shore drop-off in the near shore coastal winds is difficult to justify in our case because of the lack of observations in the coastal strip (Garreaud et al., 2011).

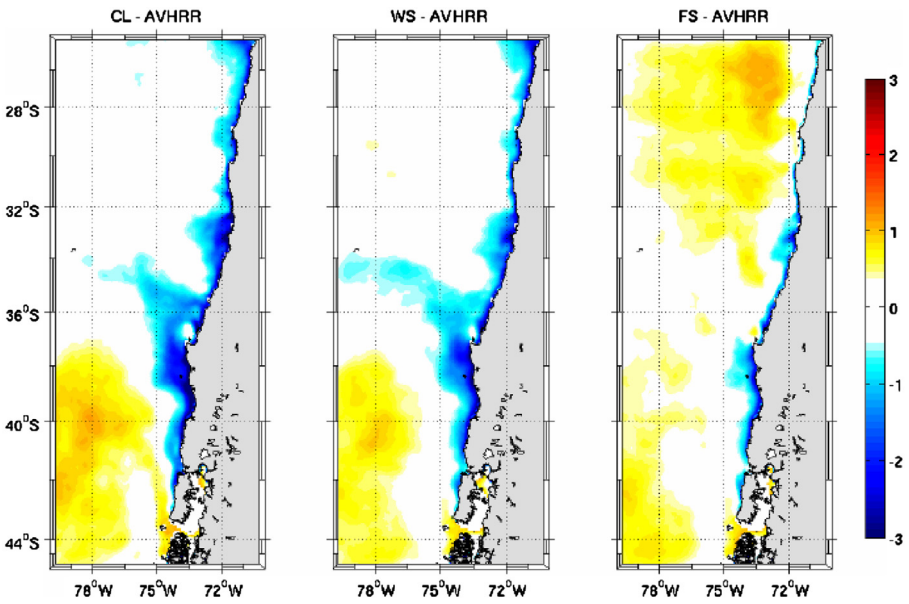

Fig. 9. Differences between the simulated summer SST in the three different simulations and the satellite observed summer SST.

As summarized in Table 4, simulated coastal SSTs are also 1–2 °C colder than in situ measurements during summer, while simulated offshore SSTs are very similar to those measured in situ at Robinson Crusoe Island. In spite of the cold bias at the coast, the model SSTs (WS and FS runs) follow quite well the observed SST anomalies, illustrated in Fig. 10 by daily time series at selected coastal stations. Multi-year correlation coefficients are significant at 95% confidence level, with values around 0.4–0.5 (Table 4) but we found values as high as 0.75 in individual years. The relatively high correlations between WS and in situ observations at the coast, in spite of the lack of realistic (daily) air-sea fluxes in this simulation, emphasize the prominent role of wind-driven upwelling cycles in coastal SST variability. In fact, the WS simulation exhibits significantly higher summer standard deviation of the coastal SST (σSST) compared with the CL one (Fig. 11). The major differences in SST variability are found in a coastal strip off south-central Chile, coincident with the region of maximum wind variability (Renault et al., 2009), where σSST in WS is about two times larger than its climatological counterpart. The cross-shore scale of the σSST maximum is about 20–30 km, corresponding to the region of strong coupling between the wind stress and SST via upwelling dynamics (e.g., Perlin et al., 2007).

On the other hand, the FS simulation is similar to WS along the coast but exhibits higher variability of the SST in the offshore region, west of about 50 km from the shore, suggesting that day-to-day SST variability over the open ocean is primarily controlled by air-sea heat fluxes. The FS values of σSST are close to those found in satellite TMI observations (Fig. 11) and agree well with the in situ measurements at Robinson Crusoe Island, while it is overestimated in coastal regions (Table 4).

4. Discussion

It is interesting to contrast the little influence of the high-frequency variable wind stress and heat fluxes on the mean near-surface currents and mean SSTs in our results, against the much higher one in coastal SST variability and ageostrophic EKE. This suggests a rather linear response of the coastal surface ocean to cycles of southerly wind strengthening (upwelling favorable) and weakening (downwelling favorable in the case of northerly winds). Assuming approximately linear relationships, the spatial response of the surface ocean to the wind variability can be described by regressing the SST and surface current fields (u_{sfc}, v_{sfc}) upon the meridional wind (*vwnd*). The point to point correlation

Table 4
Annual and summer (DJF) mean and standard deviation of in situ and simulated SST at different locations along the coast and offshore. The correlation coefficient between simulated (WS and FS runs) and observed daily SST is shown for each station considering the period 2000–2007.

Location	Data	Annual mean (°C)	Annual std (°C)	Summer mean (°C)	Summer std (°C)	Annual R	Summer R
Valparaíso 33.03° S 71.63° W	CL	13.3	1.2	14.5	0.9		
	WS	13.4	1.4	15.0	1.1	0.77	0.50 ± 0.2
	FS	13.9	1.9	16.0	1.6	0.80	0.48 ± 0.2
	In situ	13.8	1.4	15.2	1.3		
San Antonio 33.58° S 71.53° W	CL	12.6	0.8	12.8	0.7		
	WS	12.7	1.2	13.2	1.4	0.55	0.45 ± 0.3
	FS	13.0	1.5	14.0	1.9	0.67	0.54 ± 0.2
	In situ	13.6	1.5	15.2	1.3		
Talcahuano 36.70° S 73.10° W	CL	12.4	0.7	13.0	0.7		
	WS	12.3	1.1	12.9	1.3	0.48	0.43 ± 0.2
	FS	12.5	1.4	13.4	1.7	0.61	0.43 ± 0.2
	In situ	12.9	1.2	13.4	1.6		
Corral 39.87°S 73.42°W	CL	12.0	0.8	12.7	0.5		
	WS	12.0	1.3	12.9	1.6	0.58	0.42 ± 0.2
	FS	12.0	1.5	13.3	1.6	0.72	0.49 ± 0.2
	In situ	12.7	2.0	14.6	1.3		
Robinson Crusoe 33.6° S 78.8° W	CL	16.7	2.0	18.8	0.9		
	WS	16.5	2.1	18.7	0.9	0.95	0.56 ± 0.2
	FS	16.9	2.3	19.3	1.2	0.95	0.67 ± 0.2
	In situ	16.6	2.1	18.6	1.2		
	TMI	17.4	2.1	19.2	1.3		

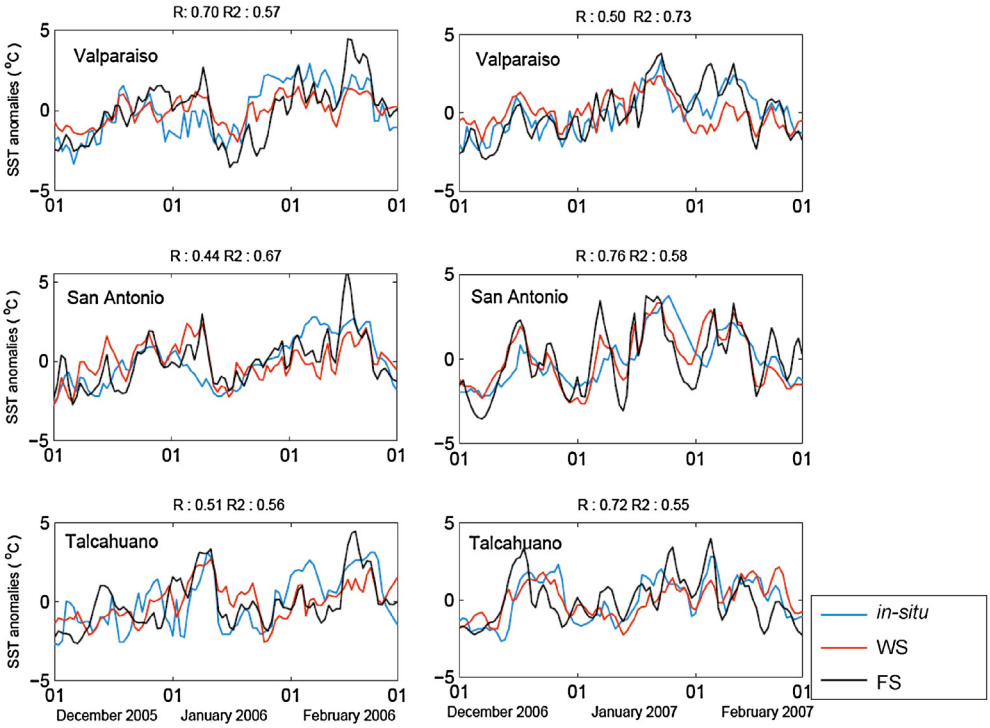

Fig. 10. Daily time series of the simulated SST in the WS (red), FS (black) and in situ observations (blue) at different locations during summer of 2006 and 2007. The correlation coefficient R is obtained from the time series of WS and observations, and the correlation coefficient R^2 is obtained from the time series of FS and observations. (For interpretation of references to color in the figure legend, the reader is referred to the web version of this article.)

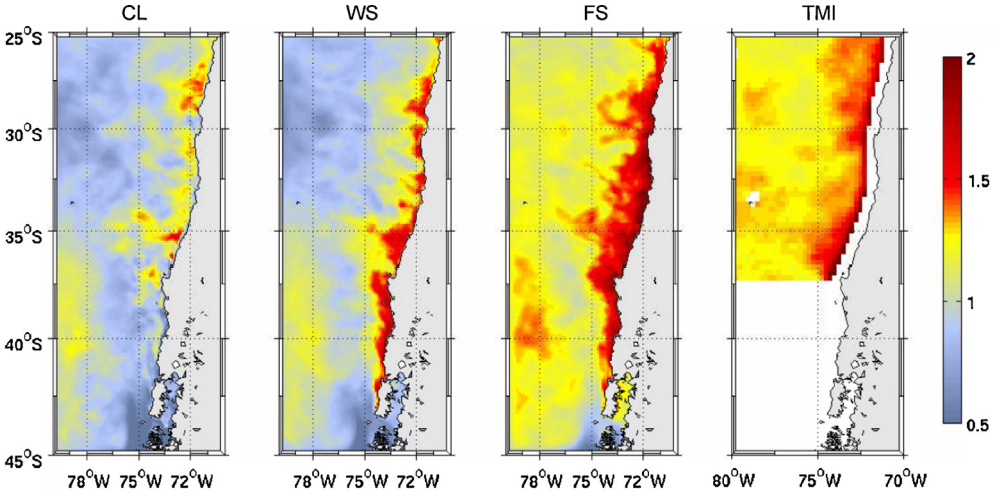

Fig. 11. Summer standard deviation of the daily sea surface temperature (°C) from the three different simulations and from the satellite TMI data.

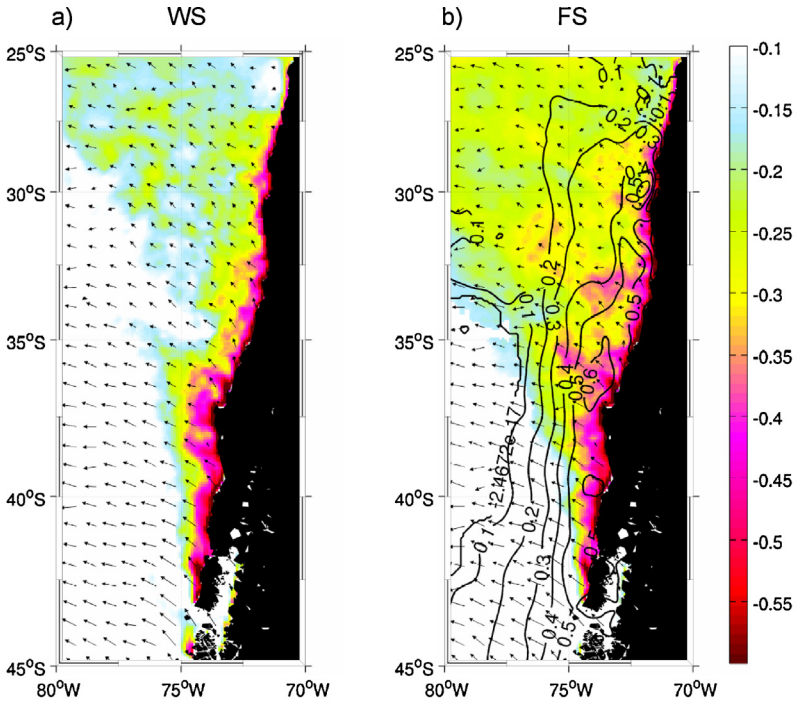

Fig. 12. Local correlation map (point to point) between meridional wind and SST (colors), meridional wind and the zonal and meridional component of surface currents (vectors). (a) WS and (b) FS includes the correlation between meridional wind and short wave radiation (contours). (For interpretation of references to color in the figure legend, the reader is referred to the web version of this article.)

(Fig. 12) between SST and meridional wind is larger than −0.5 (at one day lag) in a coastal strip about 20–30 km wide under the area of maximum wind variability. This coastally confined response of SST to variable winds is consistent with the region of strong coupling between the synoptic wind and SST via upwelling dynamics in an air-sea coupled model (Perlin et al., 2007) and with the cross-shore scale of maximum variability observed by Castelao and Barth (2005) in a field study performed off the Oregon coast during the upwelling season. On the other hand, the response of the surface ocean to atmospheric jet events is a surface flow with offshore and equatorward components (vectors in Fig. 12). The correlation between *vwnd* and v_{sfc} yielded values as high as 0.6 (at zero lag) in a very coastally confined band (10–20 km from the shore) and implies acceleration (deceleration) of the Chilean coastal current (CCC) during atmospheric jet events (relaxation), consistent with Aiken et al. (2008). The correlation between *vwnd* and u_{sfc} shows maximum negative correlations values of about −0.6 (at zero lag). In contrast with the coastally confined meridional flow and SST response, the high (*vwnd*, u_{sfc}) correlations under strong southerlies extend well offshore. These patterns and values of correlation agree well with an observational study performed off the Oregon coast (Kosro, 2005). In this research the lag of the maximum correlations between wind and surface currents was calculated in 2–12 h, which cannot be resolved by our model because of its time resolution.

In a relatively recent modeling study, Veneziani et al. (2009) compare climatological versus realistic forcings in the coastal ocean off central California. They established that the surface forcing plays a more important role than the lateral one in the California Current System simulations. In particular, the spatial resolution of the surface forcing is largely responsible for the differences in the structure and seasonal cycle of the mean upper ocean circulation between the climatological run (forced by COADS data with spatial resolution of 1°) and the realistic run (forced by COAMPS data with spatial

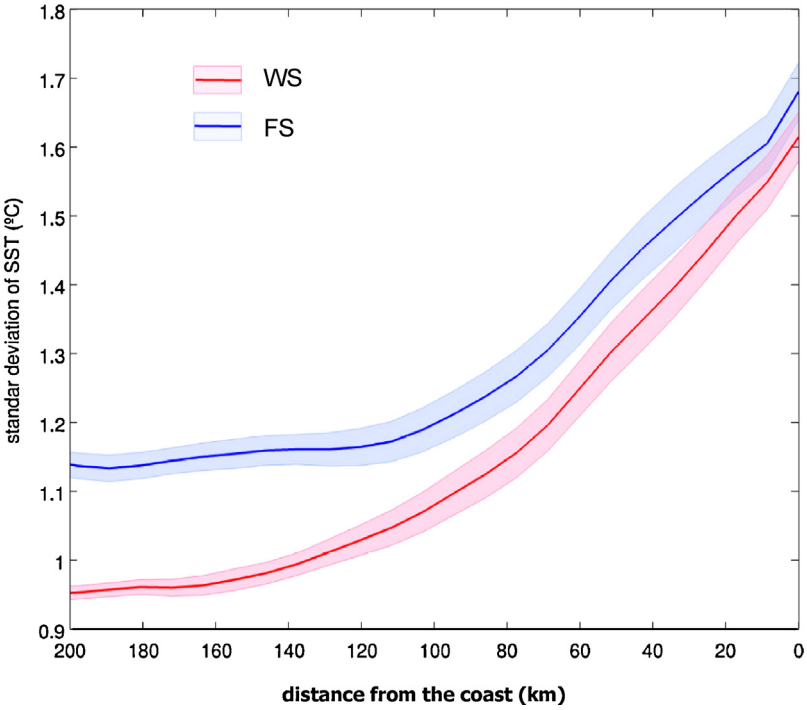

Fig. 13. Meridionally averaged (36° S–41° S) standard deviation of the SST in the WS (red line) and FS (blue line). The shaded areas indicate the confidence interval using a *t*-test at the 95% level of confidence. (For interpretation of references to color in the figure legend, the reader is referred to the web version of this article.)

resolution of 3–9 km). These results are consistent with ours in spite that we only changed the time resolution of the wind stresses while keeping their spatial resolution.

Modeling studies in the California Current System (Marchesiello et al., 2003), Benguela Current System (Penven et al., 2001) and Perú Current System (Penven et al., 2005), have provided evidence that most of the surface ocean variability is explained by intrinsic variability of the ocean arising from instabilities in the currents regardless of the presence (or absence) of high-frequency variability in the wind forcing. Both shear currents and fronts are instrumental in developing baroclinic instability (e.g. Barth, 1994; Haidvogel et al., 1991). Analysis of the energy conversion in a numerical study made by Leth and Shaffer (2001) showed that baroclinic instability is indeed a major mechanism for the generation of meanders and eddies (quasi-geostrophically balanced) off central Chile. Thus, the agreement in geostrophic EKE between our three simulations would be the result of intrinsic variability from the surface currents, especially CPC and CCC. The eddy generation at the CPC via baroclinic instability (Leth and Middleton, 2004) and the nearshore eddy generation at the CCC propagating westward (Hormazabal et al., 2004), may constitute major sources for the geostrophic EKE offshore.

The role of heat fluxes on SST variability seems to be more prominent in the offshore region, west of about 50 km from the shore. The correlation map between *vwnd* and SST for the FS run shows larger coefficients offshore but do not alter significantly these values close to the coast in comparison with WS (Fig. 12). Consequently the variability of SST in the first 30 km from the shore, in the region of maximum wind stress variability, is not significantly different between the WS and the FS (Fig. 13). In contrast, σSST offshore is significantly different between these simulations suggesting that is necessary to include synoptic variable heat fluxes to account for a realistic σSST.

The weak increase of σSST along the coast when the surface heat flux variability is included is rather puzzling. In fact, the agreement between the observed and WS-simulated coastal SST is as good as the comparison between observation and the FS results. Since the horizontal cross-shore resolution in

our simulations does not resolve upwelling cells, we have refrained from performing a coastal energy budget, as recently performed by Renault et al. (2012). Nonetheless, we offer a qualitative explanation of this apparent paradox. While the turbulent transfer coefficients for sensible and latent heat fluxes (*Qsen and Qlat*) increase during a jet event, the colder coastal SSTs foster negative (atmosphere to ocean) *Qsen*, resulting into very small *Qsen* + *Qlat* values when compared with other terms in the surface energy budget over the coastal upwelling region. On the other hand, in the real ocean, the day-to-day variability of shortwave radiation (SW) should act as a damping term in SST variability. Garreaud and Muñoz (2005) showed that the meridional wind is significant and negatively correlated with coastal cloud amount, so that coastal jet events often features clear skies which tend to heat the ocean (by the contrary, downwelling favorable winds are associated with overcast conditions). Such observational relationship between coastal *vwnd* and SW is replicated in the surface conditions used to force our model, as shown by the local correlation between these two variables (contours in Fig. 13b). Nevertheless, high mixing present during an upwelling event would render the SW flux ineffective for increasing the coastal SST. Thus SW would have little impact on σSST in FS.

5. Conclusions

In this work we have investigated the effects of the synoptic variability of the surface wind stresses and heat fluxes on the ocean off south-central Chile (35–45° S) using the Regional Ocean Model (ROMS). We performed three continuous 8-year long simulations forced by the long-term monthly mean winds (climatological run, CL), QuikSCAT (2000–2007) daily winds (synoptic wind stress run, WS) and daily winds (QuikSCAT) plus other daily atmospheric variables (2000–2007), in order to calculate surface heat fluxes thought bulk formulas (synoptic wind stress and heat fluxes run, FS). Our study focuses in the austral summer (December to February) when south-central Chile experience southerly, upwelling favorable mean wind but with substantial day-to-day variability including strong southerly jet events.

The simulated summer mean fields of upper-ocean currents and SST are very similar between the three runs and they reproduce the major observed features of the circulation in the southeast Pacific. Furthermore, the surface geostrophic EKE is similar between simulations, consistent with the idea that it is intrinsically generated by instability of the major currents. The model geostrophic EKE also agrees well with the spatial pattern observed in satellite-data, but with higher values.

In spite of the geostrophic EKE being a major component of the total EKE north of Punta Lavapié (∼37° S), the ageostrophic EKE plays an important role farther south, where the geostrophic EKE is considerably weaker due the lack of major currents. In fact, diffusivities are significantly higher (75%) when synoptic wind stress variability in surface forcing is included. These results highlight the relevance of using variable (synoptic) winds to force the ocean models if one aims to describe the turbulent component of the upper-ocean circulation, as is the case, for example, in biological models examining the dispersal of chemicals and larvae. Our results indicate that the temporal variability of the atmospheric forcing contributes to the overall energy structure, particularly in the absence of major currents which produce geostrophic EKE through baroclinic instability.

Differences between simulations using climatological and daily variable winds are also found in SST variability within the first 20–30 km offshore. The standard deviation of the daily SST in WS is about twice as large as its climatological counterpart. σSST is similar between in WS and FS, and agree well with in situ observations indicative of the prominent role of wind-driven upwelling cycles in coastal SST synoptic variability. In contrast, in the offshore region it is necessary to include daily heat flux variability to account for the SST variability observed by satellite measurements. Table 5 summarizes these major impacts of the wind stress and heat fluxes variability on the surface ocean north and south of Punta Lavapie (∼37°S). The similarities in the spatial pattern of the mean SST, currents and geostrophic EKE between the three simulations, in contrast with the much higher level of coastal SST variability and ageostrophic EKE in the runs that include synoptic variability of wind stresses and heat fluxes, is indicative of a rather linear response of the surface ocean to cycles of southerly wind strengthening and relaxation.

In order to fully describe the extent of coastal upwelling events and to perform a coastal energy budget it is necessary to significantly increase the horizontal resolution in the simulations. In addition, it has been shown that wind drop-off near the coast may play a fundamental role in upwelling

Table 5
Summary of the impacts of the of wind-stress and heat fluxes variability on surface ocean.

		Impact of wind stress variability			Impact of heat fluxes variability		
		$\frac{\text{ageos EKE}}{\text{total EKE}}$	$\bar{K}$	σSST	$\frac{\text{ageos EKE}}{\text{total EKE}}$	$\bar{K}$	σSST
North Punta Lavapié	Coast	Low	–	High	None	–	Low[a]
	Offshore	Low	Low	None	None	Low	High[a]
South Punta Lavapié	Coast	Low	–	High	None	–	None
	Offshore	High	High	None	None	Low	High

Mean SST, currents and geostrophic EKE are not included in this table because they are very similar between the three simulations

[a] Relative with respect to absolute σSST.

dynamics through Ekman pumping (Capet et al., 2004). Therefore, to solve these key aspects it would be necessary to run a validated coupled atmosphere-ocean-land model that at present is beyond the scope of this research.

Acknowledgements

CA was supported by the MECESUP 0310 Ph.D. Grant and benefited from a technical visit to the Laboratoire d'Etudes en Géophysique et Océanographie Spatiales (LEGOS, Toulouse, France) supported by ECOS-CONICYT and to the College of Oceanic and Atmospheric Sciences (COAS), Oregon State University supported by Vicerrectoría de Asuntos Académicos (VAA) and Facultad de Ciencias Físicas y Matemáticas (FCFM), Universidad de Chile. This study was partially supported by Fondecyt N°1090492. RG is supported by FONDAP-CONICYT 15110009 (CR2). The ADCP data was provided by the Center for Oceanographic Research in the Eastern South Pacific (COPAS). QuikSCAT wind data were obtained from Département d'Océanographie Spatiale, IFREMER, France. The AVHRR Oceans Pathfinder SST data were obtained from the Physical Oceanography Distributed Active Archive Center (PO.DAAC) at the NASA Jet Propulsion Laboratory.

References

Aguirre, C., Pizarro, O., Strub, P.T., Garreaud, R., Barth, J., 2012. Seasonal dynamics of the near-surface alongshore flow off central Chile. J. Geophys. Res. 117, C01006, http://dx.doi.org/10.1029/2011JC007379.
Aiken, C., Castillo, M., Navarrete, S., 2008. A simulation of the Chilean Coastal Current and associated topographic upwelling near Valparaíso, Chile. Cont. Shelf Res. 28, 2371–2381.
Antonov, J., Locarnini, R., Boyer, T., Mishonov, A., Garcia, H., 2006. In: Levitus, S. (Ed.), World Ocean Atlas 2005, vol. 2. Salinity, NOAA Atlas NESDIS, vol. 62. U.S. Gov. Print. Off, Washington, DC, p. 182.
Barth, J., 1994. Short-wavelength instabilities on coastal jets and fronts. J. Geophys. Res. 99, 16095–16115.
Batteen, M., Hu, C., Bacon, J., Nelson, C., 1995. A numerical study of the effects on wind forcing on the Chile Current System. J. Oceanogr. 51, 585–614.
Beckmann, A., Haidvogel, D., 1993. Numerical simulation of flow around a tall isolated seamount. Part I: problem formulation and model accuracy. J. Phys. Oceanogr. 23, 1736–1753.
Blanco, J.L., Thomas, A., Carr, M., Strub, P.T., 2001. Seasonal climatology of hydrographic conditions in the upwelling region off northern Chile. J. Geophys. Res. 106, 11451–11467, http://dx.doi.org/10.1029/2000JC000540.
Capet, X., Marchesiello, P., McWilliams, J., 2004. Upwelling response to coastal wind profiles. Geophys. Res. Lett. 31, L13311, http://dx.doi.org/10.1029/2004GL020123.
Capet, X., Colas, F., Penven, P., Marchesiello, P., McWilliams, J., 2008. Eddies in eastern-boundary subtropical upwelling systems eddy-resolving ocean modeling. In: Hecht, M., Hasumi, H. (Eds.), AGU Monograph.
Carr, S., Capet, X., McWilliams, J., Pennington, T., Chavez, F., 2008. The influence of diel vertical migration on zooplankton transport and recruitment in an upwelling region. Fish. Oceanogr. 16, 1–15, http://dx.doi.org/10.1111/j.1365-2419.2007.00447.x.
Castelao, R., Barth, J., 2005. Coastal ocean response to summer upwelling favorable winds in a region of alongshore bottom topography variations. J. Geophys. Res. 110, C10S04, http://dx.doi.org/10.1029/2004JC002429.
Chaigneau, A., Pizarro, O., 2005. Mean surface circulation and mesoscale turbulent flow characteristics in the eastern South Pacific from satellite tracked drifters. J. Geophys. Res. 110, C05014, http://dx.doi.org/10.1029/2004JC002628.
Da Silva, A., Young, C., Levitus, S., 1994. Atlas of surface marine data 1994. Algorithms and Procedures, Technical Report, vol. 1. Natl. Oceanogr. and Atmos. Admin., Silver Spring, MD.
Ducet, N., Le Traon, P., Reverdin, G., 2000. Global high-resolution mapping of ocean circulation from TOPEX/Poseidon and ERS-1 and -2. J. Geophys. Res. 105 (C8), http://dx.doi.org/10.1029/2000JC900063.
Dunn, J.R., Ridgway, K.R., 2002. Mapping ocean properties in regions of complex topography. Deep Sea Res. 49 (3), 591–604.

Figueroa, D., Moffat, C., 2000. On the influence of topography in the induction of coastal upwelling along Chilean coast. Geophys. Res. Lett. 27 (23), http://dx.doi.org/10.1029/1999GL011302.
Ekman, V.W., 1905. On the influence of the earth' rotation in ocean currents. Arch. Math. Astron. Phys. 2, 1–52.
Food and Agriculture Organization, 2004. El estado mundial de la pesca y la acuicultura 2004, Rep. 92-5-205177-5, Roma.
Fuenzalida, R., Schneider, W., Garcés-Vargas, J., Bravo, L., 2008. Satellite altimetry data reveal jet-like dynamics of the Humboldt Current. J. Geophys. Res. 113, C07043, http://dx.doi.org/10.1029/2007JC004684.
Garreaud, R., Muñoz, R., 2005. The low level jet off the west coast of subtropical South America: structure and variability. Mon. Weather Rev. 133, 2246–2261.
Garreaud, R., Rutllant, J.A., Fuenzalida, H., 2002. Coastal lows along the subtropical west coast of South America: Mean structure and evolution. Mon. Weather Rev. 130, 75–88.
Garreaud, R., Rutllant, J.A., Muñoz, R., Rahn, D., Ramos, M., Figueroa, D., 2011. VOCALS-CUpEx: the Chilean Upwelling Experiment. Atmos. Chem. and Phys 11, 2015–2029, http://dx.doi.org/10.5194/acp-11-2015-2011.
Haidvogel, D.B., Beckman, A., Hedstrom, K.S., 1991. Dynamical simulation of filament formation and evolution in the coastal transition zone. J. Geophys. Res. 96, 15017–15040.
Hormazabal, S., Shaffer, G., Leth, O., 2004. Coastal transition zone off Chile. J. Geophys. Res. 109, C01021, http://dx.doi.org/10.1029/2003JC001956.
Kalnay, E., Kanamitsu, M., Kistler, R., Collins, W., Deaven, D., Gandin, L., Iredell, M., Saha, S., White, G., Woollen, J., Zhu, Y., Chelliah, M., Ebisuzaki, W., Higgins, W., Janowiak, J., Mo, K.C., Ropelewski, C., Wang, J., Leetmaa, A., Reynolds, R., Jenne, R., Joseph, D., 1996. The NCEP/NCAR 40-year reanalysis project. Bull. Am. Meteor. Soc. 77 (3), 437–470.
Kosro, P.M., 2005. On the spatial structure of coastal circulation off Newport, Oregon, during spring and summer 2001 in a region of varying shelf width. J. Geophys. Res. 110, C10S06, http://dx.doi.org/10.1029/2004JC002769.
Kundu, P., Cohen, I., 2000. Fluid Mechanics, 2nd ed. Elsevier, New York, pp. 730.
Large, W., McWilliams, J., Doney, S., 1994. Oceanic vertical mixing: a review and a model with a nonlocal boundary layer parameterizations. Rev. Geophys. 32, 363–403.
Letelier, J., Pizarro, O., Nuñez, S., 2009. Seasonal variability of coastal upwelling and the upwelling front off central Chile. J. Geophys. Res. 114, C12009, http://dx.doi.org/10.1029/2008JC005171.
Leth, O., Middleton, J., 2004. A mechanism for enhanced upwelling off Central Chile: eddy advection. J. Geophys. Res. 109, C12020, http://dx.doi.org/10.1029/2003JC002129.
Leth, O., Shaffer, G., 2001. A numerical study of the seasonal variability in the circulation off central Chile. J. Geophys. Res. 106, 22229–22248, http://dx.doi.org/10.1029/2000JC000627.
Locarnini, R., Mishonov, A., Antonov, J., Boyer, T., Garcia, H., 2006. In: Levitus, S. (Ed.), World Ocean Atlas 2005 vol. 1. Temperature, NOAA Atlas NESDIS vol. 61. U.S. Gov. Print. Off, Washington, DC, 182 pp.
Marchesiello, P., McWilliams, J., Shchepetkin, A., 2001. Open boundary conditions for long-term integration of regional oceanic models. Ocean Modell. 3, 1–21.
Marchesiello, P., McWilliams, J., Shchepetkin, A., 2003. Equilibrium structure and dynamics of the California Current system. J. Phys. Oceanogr. 33, 753–783.
Mesias, J., Matano, R., Strub, P.T., 2001. A numerical study of the upwelling circulation off central Chile. J. Geophys. Res. 106, 19611–19623, http://dx.doi.org/10.1029/2000JC000649.
Mesias, J., Matano, R., Strub, P.T., 2003. Dynamical analysis of the upwelling circulation off central Chile. J. Geophys. Res. 108 (3085), http://dx.doi.org/10.1029/2001JC001135.
Montecino, V., Strub, T., Chavez, F., Thomas, A., Tarazona, J., Baumgartner, T., 2006. In: Robinson, A.R., Brink, K.H. (Eds.), Bio-physical Interactions off Western South-America in The Sea vol. 14, The Global Coastal Ocean: Regional Studies and Syntheses. Harvard Univ. Press, Cambridge, MA, pp. 329–390.
Montecinos, A., Muñoz, R., Garreaud, R., Arraigada, A., Conejero, C., Morales, J., Burger, F., Sanchez, E., Vizcarra, A., 2011. Experimiento de Surgencia Costera en el Golfo de Arauco (CUPEX-II). Segundo Congreso de Oceanografía Física. Meteorología y Clima Coquimbo, Chile.
Muñoz, R., Garreaud, R., 2005. Dynamics of the low level jet off the west coast of subtropical South America. Mon. Weather Rev. 133, 3661–3677.
Penven, P., Roy, C., Lutjeharms, J., Colin de Verdière, A., Johnson, A., Shillington, F., Fréon, P., Brundrit, G., 2001. A regional hydrodynamic model of the Southern Benguela. S. Afr. J. Sci. 97, 472–476.
Penven, P., Echevin, V., Pasapera, J., Colas, F., Tam, J., 2005. Average circulation, seasonal cycle and mesoscale dynamics of the Perú Current System: a modeling approach. J. Geophys. Res. 110, C10021, http://dx.doi.org/10.1029/2005JC002945.
Perlin, N., Skyllingstad, E., Samelson, R., Barbour, P., 2007. Numerical simulation of air–sea coupling during coastal upwelling. J. Phys. Oceanogr. 37, 2081–2093, http://dx.doi.org/10.1175/JPO3104.1.
Pizarro, O., Shaffer, G., Dewitte, B., Ramos, M., 2002. Dynamics of seasonal and interanual variability of the Peru–Chile undercurrent. Geophys. Res. Lett. 29, 12, http://dx.doi.org/10.1029/2002GL 014790.
Putrasahan, D., Miller, A., Seo, H., 2013. Regional coupled ocean-atmosphere downscaling in the Southeast Pacific: impacts on upwelling, mesoscale air-sea fluxes and ocean eddies. Ocean Dynamics 63, 463–488, http://dx.doi.org/10.1007/s10236-013-0608-2.
Renault, L., Dewitte, B., Falvey, M., Garreaud, R., Echevin, V., Bonjean, F., 2009. Impact of the atmospheric coastal jet off central Chile on sea surface temperature from satellite observations (2000–2007). J. Geophys. Res. 114, C08006, http://dx.doi.org/10.1029/2008JC005083.
Renault, L., Dewitte, B., Marchesiello, P., Illig, S., Echevin, V., Cambon, G., Ramos, M., Astudillo, O., Minnis, P., Ayers, K., 2012. Upwelling response to atmospheric coastal jets off central Chile: a modeling study of the October 2000 event. J. Geophys. Res. 117, C02030, http://dx.doi.org/10.1029/2011JC007446.
Ridway, K.R., Dunn, J.R., Wilkin, J.L., 2002. Ocean interpolation by four-dimensional least squares—applications to the waters around Australia. J. Atmos. Ocean Technol. 19 (9), 1357–1375.
Rutllant, J., Montecino, V., 2002. Multiscale upwelling forcing cycles and biological response off north-central Chile. Rev. Chil. Hist. Nat. 75, 217–231.
Saavedra, N., Foppiano, A., 1992. Monthly mean pressure model for Chile. Int. J. Climat. 12, 469–480.

Saha, S., 2010. The NCEP climate forecast system reanalysis. Bull. Am. Meteor. Soc. 91, 1015–1057.
Shaffer, G., Pizarro, O., Djurfeldt, L., Salinas, S., Rutllant, J., 1997. Circulation and low-frequency variability near the Chile coast: remotely forced fluctuations during the 1991–1992 El Niño. J. Phys. Oceanogr. 27, 217–235.
Shaffer, G., Hormazábal, S., Pizarro, O., Djurfeldt, L., Salinas, S., 1999. Seasonal and interannual variability of currents and temperature over the slope off central Chile. J. Geophys. Res. 104, 29951–29961, http://dx.doi.org/10.1029/1999JC900253.
Shchepetkin, A., McWilliams, J., 2003. A method for computing horizontal pressure–gradient force in an ocean model with nonaligned vertical coordinate. J. Geophys. Res. 108C3 (3090), http://dx.doi.org/10.1029/2001JC001047.
Shchepetkin, A., McWilliams, J., 2005. The regional oceanic modeling system (ROMS): a split-explicit, free-surface, topography-following-coordinate oceanic model. Ocean Model. 9, 347–404.
Smith, W., Sandwell, D., 1997. Global seafloor topography from satellite altimetry and ship depth soundings. Science 277, 1957–1962.
Sobarzo, M., Bravo, L., Donoso, D., Garces-Vargas, J., Schneider, W., 2007. Coastal upwelling and seasonal cycle that influence the water column over the continental shelf off central Chile. Prog. Oceanogr. 75, 363–382.
Sobarzo, M., Bravo, L., Moffat, C., 2010. Diurnal-period, wind forced ocean variability on the inner shelf off Concepción, Chile. Cont. Shelf Res. 30, 2043–2056, http://dx.doi.org/10.1016/j.csr. 2010.10.004.
Song, Y., Haidvogel, D., 1994. A semi-implicit ocean circulation model using a generalized topography following coordinate system. J. Comput. Phys. 115, 228–248.
Strub, P.T., Montecino, V., Rutllant, J., Salinas, S., 1998. Coastal ocean circulation off western south America. In: Robinson, A.R., Brink, K.H. (Eds.), The Sea. The Global Coastal Ocean: Regional Studies and Syntheses, vol. 11. John Wiley, New York, pp. 273–314.
Strub, P.T., Mesias, M., James, C., 1995. Altimeter observations of the Perú-Chile countercurrent. Geophys. Res. Lett. 22, 211–214, http://dx.doi.org/10.1029/94GL02807.
Veitch, J., Penven, P., Shillington, F., 2010. Modeling equilibrium dynamics of the Benguela Current system. J. Phys. Oceanogr. 40, 1942–1964, http://dx.doi.org/10.1175/2010JPO4382.1.
Veneziani, M., Edwards, C.A., Doyle, J.D., Foley, D., 2009. A central California coastal ocean modeling study: 1. Forward model and the influence of realistic versus climatological forcing. J. Geophys. Res. 114, http://dx.doi.org/10.1029/2008JC004774.
Wentz, F.J., Gentemann, C., Smith, D., Chelton, D., 2000. Satellite measurements of sea surface temperature through clouds. Science 288, 847–850, http://dx.doi.org/10.1126/science.288.5467.847.